

Communication

Hierarchical Multiple Precursors Induced Heterogeneous Structures in Super Austenitic Stainless Steels by Cryogenic Rolling and Annealing

Duo Tan ^{1,*} , Bin Fu ^{1,*}, Wei Guan ¹, Yu Li ¹, Yanhui Guo ¹, Liqun Wei ¹ and Yi Ding ²¹ School of Materials Science and Engineering, Shanghai Institute of Technology, Shanghai 201418, China² Baowu Special Metallurgy Co., Ltd., Shanghai 200940, China

* Correspondence: tanduo2023@163.com (D.T.); bin_fu@163.com (B.F.)

Abstract: Multiple deformed substructures including dislocation cells, nanotwins (NTs) and martensite were introduced in super austenitic stainless steels (SASSs) by cryogenic rolling (Cryo-R, 77 K/22.1 mJ·m⁻²). With the reduction increasing, a low stacking fault energy (SFE) and increased flow stress led to the activation of secondary slip and the occurrence of NTs and martensite nanolaths, while only dislocation tangles were observed under a heavy reduction by cold-rolling (Cold-R, 293 K/49.2 mJ·m⁻²). The multiple precursors not only possess variable deformation stored energy, but also experience competition between recrystallization and reverse transformation during subsequent annealing, thus contributing to the formation of a heterogeneous structure (HS). The HS, which consists of bimodal-grained austenite and retained martensite simultaneously, showed a higher yield strength (~1032 MPa) and a larger tensile elongation (~9.1%) than the annealed coarse-grained Cold-R sample. The superior strength–ductility and strain hardening originate from the synergistic effects of grain refinement, dislocation and hetero-deformation-induced hardening.

Keywords: super austenitic stainless steel; cryogenic rolling; heterogeneous structure; microstructure; mechanical properties



Citation: Tan, D.; Fu, B.; Guan, W.; Li, Y.; Guo, Y.; Wei, L.; Ding, Y.

Hierarchical Multiple Precursors Induced Heterogeneous Structures in Super Austenitic Stainless Steels by Cryogenic Rolling and Annealing. *Materials* **2023**, *16*, 6298. <https://doi.org/10.3390/ma16186298>

Academic Editors: Andrea Di Schino and Claudio Testani

Received: 18 August 2023

Revised: 10 September 2023

Accepted: 18 September 2023

Published: 20 September 2023



Copyright: © 2023 by the authors. Licensee MDPI, Basel, Switzerland. This article is an open access article distributed under the terms and conditions of the Creative Commons Attribution (CC BY) license (<https://creativecommons.org/licenses/by/4.0/>).

1. Introduction

Super austenitic stainless steels (SASSs) have been widely used in extremely harsh service environments such as flue gas desulfurization, seawater desalination, and the petrochemical industry [1,2]. However, the yield strength (YS) of SASS is relatively low due to its large grain size and low dislocation density, which strongly limit its further applications. Microstructure refinement is an effective method to improve its YS, and some severe plastic deformation (SPD) methods such as dynamic plastic deformation (DPD) [3,4] and surface mechanical grinding treatment (SMGT) [5,6] are often conducted to obtain the nanostructure; however, they are always accompanied by a significant deterioration in ductility. On this basis, the strategy of heterogeneous structures (HSs), such as bimodal, harmonic and hierarchical lamellar structures, was proposed to achieve a good combination of strength and ductility [7–9]. Generally, the commonly available approach to obtain bulk HS in conventional austenitic stainless steels (ASSs) is through annealing after severe cold deformation [10]. The heterogeneity was obtained due to a competitive process between the reverse transformation of strain-induced martensite and the recrystallization of a dislocation-cell-type structure [3], thus resulting in a hierarchical distribution of grain sizes, from tens of nanometers to several micro-meters. However, the deformation mode of the studied SASS at an ambient temperature is mainly dislocation-dominated shear band, owing to a heavy alloying of Mo and N and increased stacking fault energy (SFE) [11,12] during cold deformation. The homogeneous rolled substructure hardly contributes to the HS formation due to a similar deformation stored energy for the nucleation and

growth of recrystallization [13]. Additionally, dislocation annihilation during recovery or recrystallization impedes structural refinement by walls or cells [14], resulting in low YS.

Recently, an innovative cryogenic rolling (Cryo-R) procedure was performed in conventional ASSs to obtain nanostructures with high YS [15]. An effective inhibition of dislocation recovery during Cryo-R contributed to a larger stored energy and higher driving force for the nucleation of recrystallization compared to the traditional Cold-R [16]. However, most investigations have ignored the advantage of Cryo-R in activating multiple deformed substructures, including dislocation tangles, mechanical twins and deformation-induced martensite (DIM) [12,17], due to a temperature-controlled variable SFE, since the diversity of precursor is a crucial factor in obtaining a heterogeneous grain-size distribution. Firstly, the recrystallization dynamics are closely related to the nucleation site, such as the dislocation cell and twin boundaries [18–20]. Some studies have shown that the nanocrystalline nucleation rate in the grain boundary, nanotwin and shear band regions of precursors was faster than that in the dislocation region of coarse crystals during annealing [21,22]. Moreover, the reversed austenite grains may inherit the lath morphology of the DIM after the reverse transformation [23] compared to the equiaxed recrystallized grains. However, little attention has been paid to the effects of deformed precursors with complex substructures in obtaining HS. The motivation of the present study is to investigate the relationship among the HSs, deformation modes and the evolution of multiple precursors during Cryo-R, which provides a guiding design of high-strength SASS for extreme applications.

2. Materials and Methods

In this work, the chemical composition of SASS was listed as follows: 0.024 C, 0.38 Si, 0.98 Mn, 0.027 P, 0.004 S, 16.9 Cr, 13.23 Ni, 5.3 Mo, 0.13 N and balanced Fe, wt. %. The cast ingots were cut into $5 \times 30 \times 100$ mm samples and then heated in a muffle furnace at 1200 °C for 2 h for the solution treatment, followed by water cooling. A multi-pass Cryo-R procedure was conducted in a rolling mill ($\phi 180$ mm) with different total reductions of 30%, 50%, and 70%. Before Cryo-R, the iron oxide scale on the surface was removed with coarse sandpaper, and a soak for 15 min was made at a cryogenic temperature. For comparison, Cold-R samples with a 70% reduction according to the same rolling parameters were prepared. Moreover, the 70% rolled samples were subsequently annealed at 700 °C for 10 min. The X-ray (XRD, D/max 2200 PC; Shimadzu, Kyoto, Japan) analysis was conducted by Cu target $K\alpha$ rays with a scan rate of $2^\circ/\text{min}$ from 40° to 100° . The Vickers hardness values were performed on a 402SXV hardness tester for 5 s with 300 g of load retention. For transmission electron microscope (TEM) observation, the samples were thinned by double-spray electrolysis, and the double-spray liquid was a perchloric acid alcohol solution (voltage and temperature were 30 V and -30°C , respectively). Then, the samples were observed by FEI TECNAI TEM (FEI, Lexington, KY, USA). The electron backscatter diffraction (EBSD) characterizations of the RD-ND surface were investigated by MIR3 high-resolution scanning electron microscopy at a 20 kV acceleration voltage.

3. Results and Discussion

Figure 1 shows the evolution of the XRD patterns and Vicker hardness values of SASS before and after Cryo/Cold-R with different reductions. The diffraction peaks of all samples showed a single austenitic phase structure, which possesses a strong mechanical stability even at cryogenics. However, the DIM was observed in the Cryo-R samples by TEM analysis later; this inaccuracy was mainly due to its low volume fraction and nano-lath size. Moreover, the hardness value showed a monotonous increasing tendency with the cryogenic reduction increasing. However, it increased slowly during the early rolling process but showed a high increasing rate after the 30% reduction, which demonstrated the change in deformation modes. In addition, the hardness of the Cryo-R sample was obviously higher than that of the Cold-R sample at an equivalent strain of 70%, indicating

that the former possessed a higher deformation stored energy due to the inhibition of dislocation recovery.

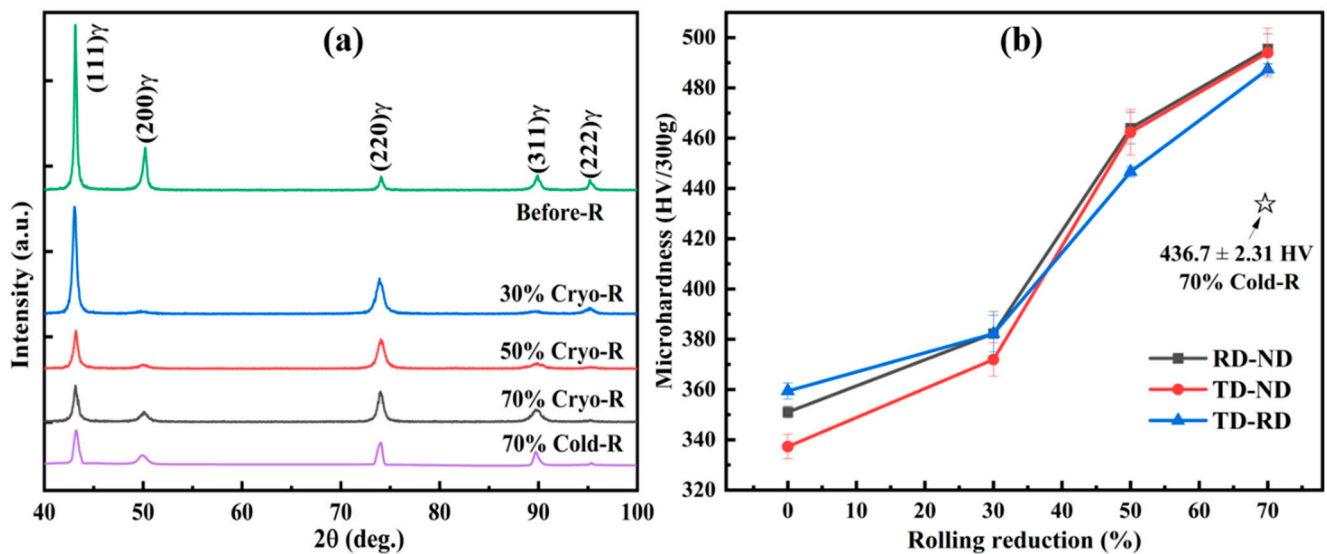


Figure 1. (a) The XRD patterns and (b) Vickers hardness values of SASS before and after Cryo/Cold-R with different reductions.

Figure 2 depicts the typical TEM images of the Cryo-R SASS sample after 30% and 50% reductions. At low strains, a large number of slip bands were accompanied with dislocation cells or walls, and the motion of dislocations continuously crossed the matrix [24]. The corresponding selected area electron diffraction spots (SAED) shown in Figure 2a illustrate a single austenitic structure in this area, indicating that the martensitic transformation hardly occurs in the early cryogenic deformation stage. Furthermore, several nanotwins (NTs) were also observed, which was confirmed by SAED in Figure 2b. At low temperatures, the motion of dislocations was suppressed and instead the formation of twins was strongly promoted due to a decreased SFE [25]. According to the statistics, the average thickness of T/M lamellae was ~24.64 nm. With strain progressing to 50%, the further evolution of dislocation walls and cells not only inhibited dislocation slip, but also promoted an effective grain refinement [26]. More importantly, the enhanced nucleation driving force led to a significantly increased number density of NTs (Figure 2d), and the average size of T/M lamellar thickness was reduced to ~16.43 nm.

When the rolling reduction increased to 70%, the austenitic grains were strongly refined; the ring-shaped SAED (Figure 3a) also indicated that the number of high-angle grain boundaries [27] obviously increased with a high degree of lattice distortion [28]. In addition, some special parallelogram regions of shear band interactions could be observed, and their interactions acted as the nucleation sites of the deformation-induced α' martensite, which possessed a block morphology with a grain size of several micro-meters.

Moreover, some high-density secondary NTs could be observed between slip bands, and they showed a very thin T/M lamellar thickness of ~4.84 nm. The generation of secondary NTs was mainly caused by the strain gradient between adjacent grain boundaries [29]. Simultaneously, some nano-lath ϵ martensite also formed in the deformed ultra-fine grains (Figure 3c), which might be attributed to a limited dislocation storage and motion ability. In contrast, the formation of NTs or martensite was hardly observed in the Cold-R samples and only a large number of dislocation structures was evident in the grain interior.

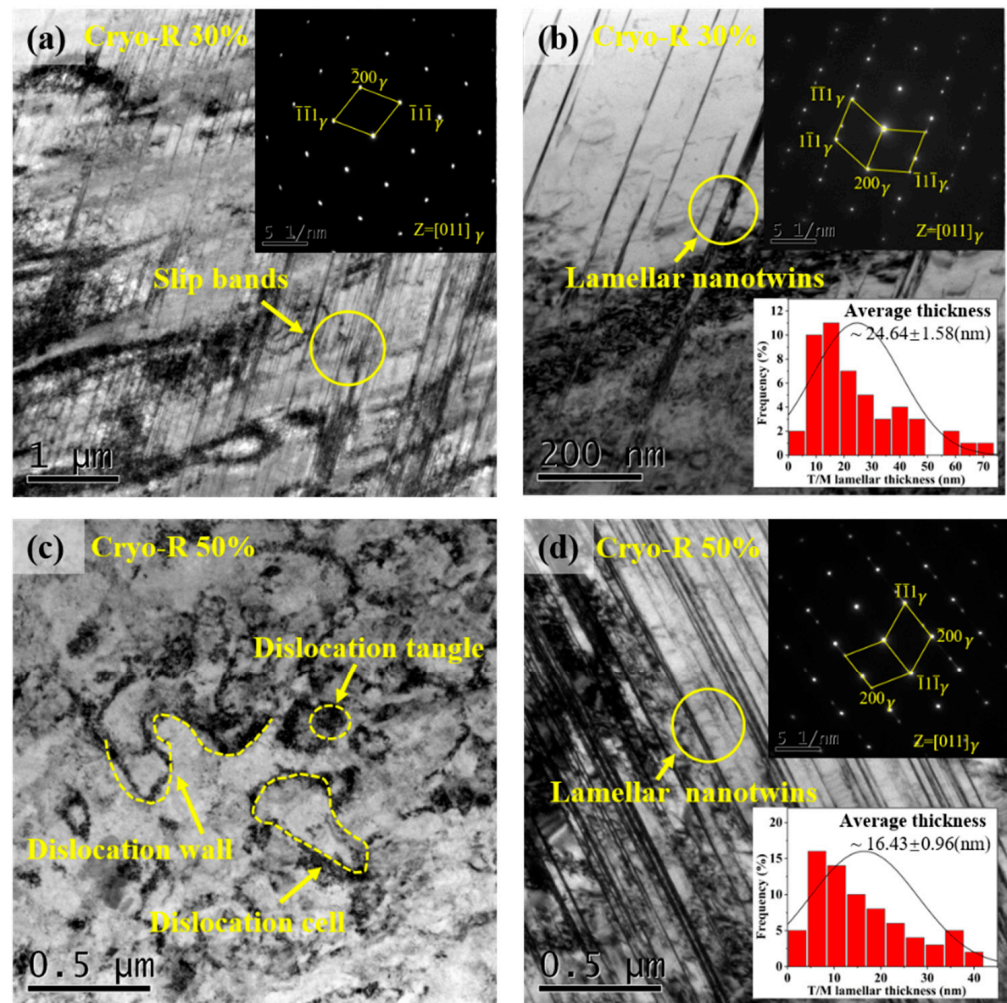


Figure 2. TEM micrographs of the SASSs after Cryo-R: (a) bright field image (BF) showing slip bands with 30% reduction; (b) BF showing lamellar NTs with 30% reduction; (c) BF showing dislocation structural with 50% reduction; (d) BF showing the lamellar NTs with 50% reduction.

As illustrated above, a hierarchical multiple deformed substructure, combined with dislocation cells, NTs, ϵ martensite and α' martensite, could be found in the SASS during the cryogenic rolling process. The dislocation cells and walls dominate at low strains and the enhanced planar slip leads to the formation of slip bands. With the deformation progressing to a medium stage, a limited dislocation motion ability and increased flow stress result in the occurrence of high-density deformation twins and secondary slip bands, contributing to an obvious grain-refinement effect. Furthermore, the strain-induced α' martensite nucleates in the interactions of shear bands and some stress-assisted ϵ martensite forms within the dislocation cell boundaries at large strains. The generation of such a multi-stage deformation mechanism is closely related to the temperature-controlled SFE and the conditions for the twin and martensite formation. Firstly, using the previously reported thermodynamic model by Saeed-Akbari et al. [30], and considering the change in SFE Γ by temperature besides alloy composition and grain size, Equation (1) is expressed as follows:

$$\Gamma = 2\rho\Delta G^{\gamma\rightarrow\epsilon} + 2\sigma^{\gamma/\epsilon} + 2\rho\Delta G_{ex} \quad (1)$$

where ρ is the molar surface density along $\{111\}$ planes and $\Delta G^{\gamma\rightarrow\epsilon}$ and $\sigma^{\gamma/\epsilon}$ are the free energy change and interfacial energy; ΔG_{ex} is the excess free energy due to the grain-size effect. Thus, the SFE values of the studied SASS are calculated as $\sim 49.2 \text{ mJ}\cdot\text{m}^{-2}$ and $\sim 22.1 \text{ mJ}\cdot\text{m}^{-2}$ at 293 K and 77 K, respectively. Moreover, according to the classic dislocation

theory, the critical shear stress (CRSS) for the formation of the deformation twin can be expressed as follows [31]:

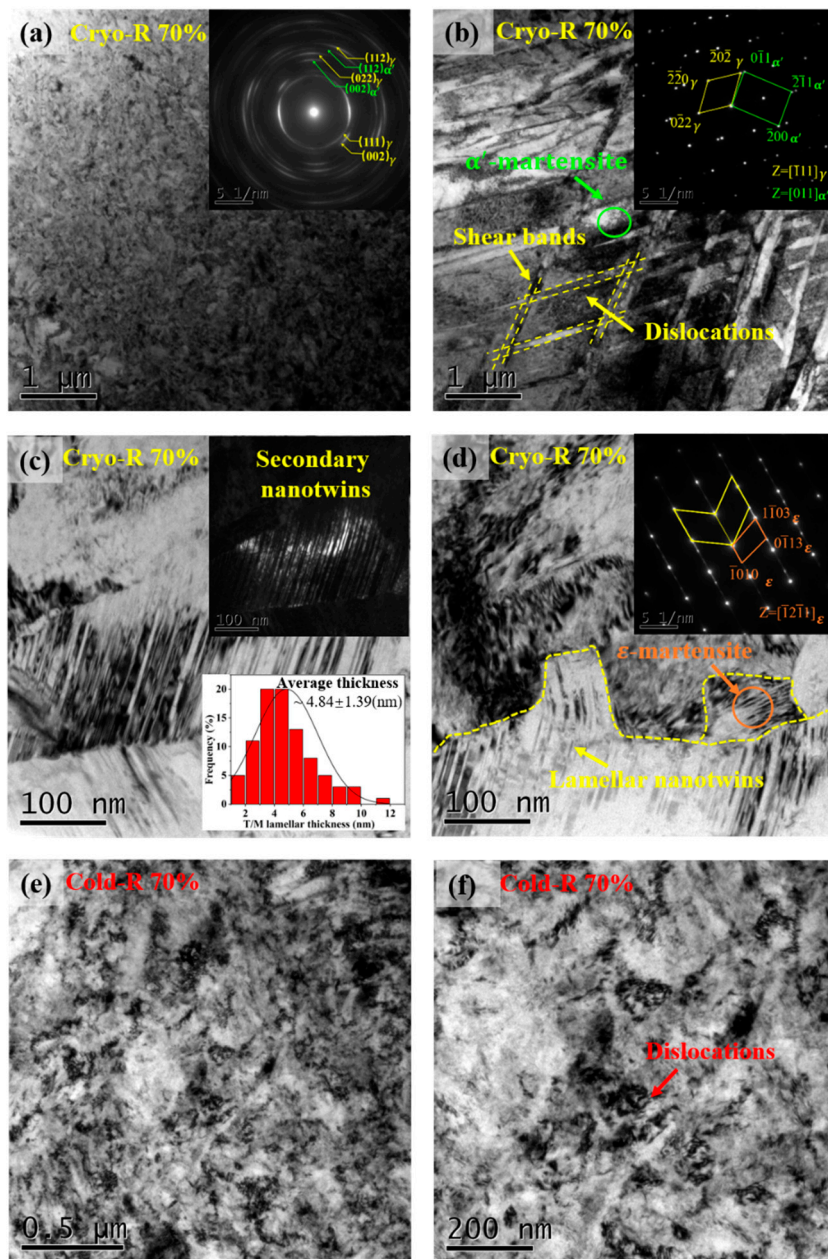


Figure 3. TEM micrographs of Cryo/Cold-R sample with 70% reduction: (a) BF and corresponding SAED; (b) BF showing the shear bands, α' martensite; (c) BF showing the lamellar NTs, ϵ -martensite; (d) TEM micrograph of Cold-R sample with 70% reduction; (e) BF showing the matrix; (f) BF showing the dislocations.

$$\tau_{twin} = \frac{2\Gamma}{b_p} \tag{2}$$

where Γ is the SFE value, and b_p is the Burgers vector of partial dislocations. Also, the driving force for the martensitic formation can be expressed as follows:

$$-\Delta G^{\gamma \rightarrow \epsilon} + \tau_{MT} s V_m = \int_{\gamma}^{\epsilon} T dS \tag{3}$$

where τ_{MT} is the CRSS for the onset of $\gamma \rightarrow \varepsilon$ transformation, s is the homogeneous transformation shear strain, V_m is the molar volume of austenite, $\int_{\gamma}^{\varepsilon} T dS$ is the change in entropy during $\gamma \rightarrow \varepsilon$ transformation. The parameter details are referred to in the previous work [32]. Thus, the CRSS values of twinning and martensite can be calculated as ~ 671 MPa and ~ 630 MPa at 293 K, and ~ 301 MPa and ~ 350 MPa at 77 K, respectively; that is, a lower CRSS results in the sequence of nanotwins and martensite when deformed at cryogenics, while they hardly form at RT due to the high CRSS values.

Figure 4 shows the microstructural characteristic of annealed SASS after Cryo-R and Cold-R, including the inverse pole figures (IPFs), phase distribution maps and grain-size distributions from EBSD. A partial recrystallization process exists in both samples due to an insufficient annealing time. The annealed Cryo-R samples show a complex phase constitution of retained martensite and recrystallized and reversed austenite, which possesses a bimodal grain-size distribution, that is, ultrafine grains ($\sim 0.57 \mu\text{m}$) and coarse grains ($\sim 2 \mu\text{m}$). The reverse transformation of strain-induced martensite cannot be completed due to a low migration distance of γ/α' phase boundary during the short-term annealing at 700°C . However, the annealed Cold-R samples show a fully austenitic microstructure, consisting of coarse recovered grains and fine recrystallized grains, and their average grain size is higher than that of annealed Cryo-R samples. Compared with the Cold-R samples, the annealed Cryo-R samples show a larger heterogeneity and wider grain-size distributions; this phenomenon can be attributed to the hierarchical multiple precursors which experience competition among reverse transformation, recrystallization and recovery. For instance, the reversed austenite is prone to inherit the nano-lath morphology of martensite [33], while the growth of recrystallized grains in the deformation twin is strongly suppressed by the twin plane [34], and they exhibit a significantly smaller grain size than those nucleating in the dislocation cell boundaries. Moreover, the Cryo-R process leads to higher deformation stored energy than the Cold-R at an equivalent strain [35], which facilitates the improvement in the nucleation rate and contributes to a smaller average grain size [29].

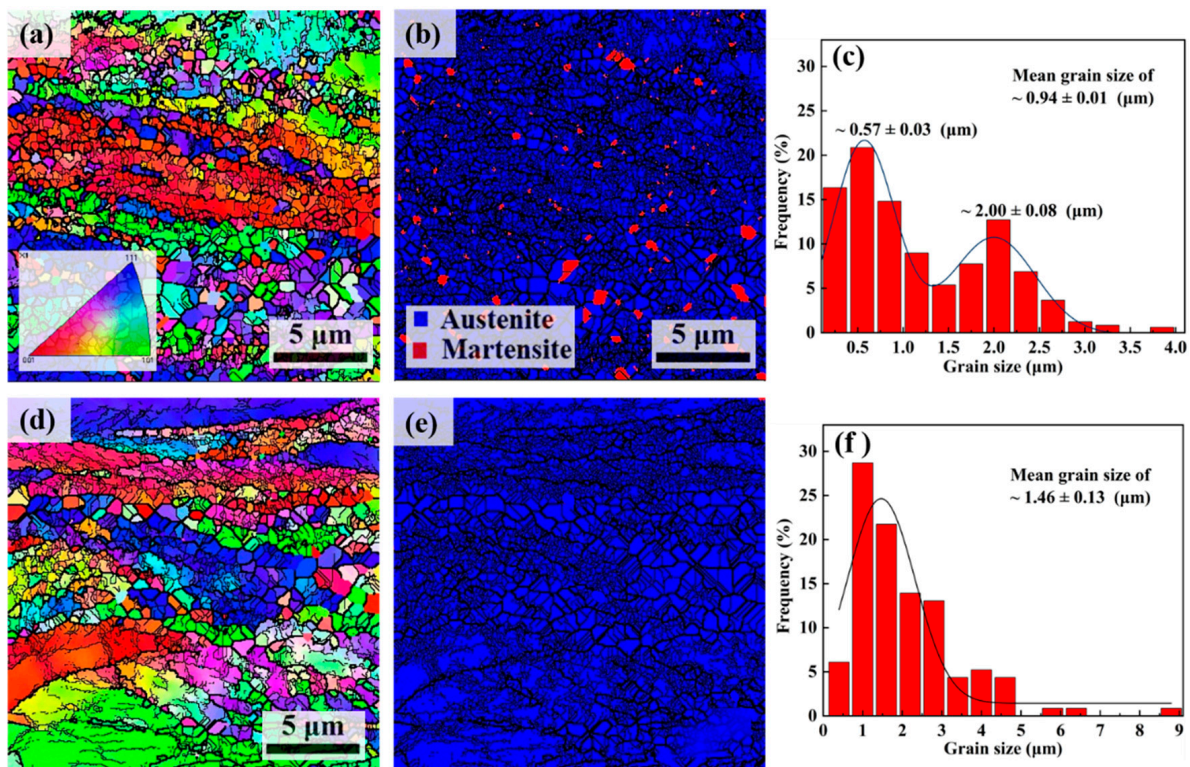


Figure 4. IPF maps, phase distribution maps and grain-size distribution of annealed SASS after (a–c) Cryo-R and (d–f) Cold-R.

Figure 5 shows the engineering stress–strain and corresponding strain-hardening curves of the rolled and annealed SASS specimens. For the rolled specimens (a and c), the Cryo-R samples show higher YS and ultimate tensile strength (UTS) values but similar total elongation (TEL) compared with those of the Cold-R samples, which originate from a higher dislocation density (see the Supplementary Material) due to the inhibition of dislocation recovery at cryogenics. Moreover, the annealed Cold-R samples show an improved TEL value under the sacrifice of tensile strength compared with the rolled state, that is, the strength–ductility trade-off. However, the annealed Cryo-R sample shows simultaneously higher UTS and TEL values (~ 1556.36 MPa, $\sim 9.1\%$) than those of the rolled state (~ 1448 MPa, $\sim 4.93\%$), and the YS only decreases a little. Moreover, although the strain-hardening (SH) rate showed a decreasing tendency with deformation progressing, the SH value of the annealed Cryo-R sample was significantly higher than that of the annealed Cold-R sample during the whole tensile stage. As shown in Figure 5c, the superior strength–ductility synergy of the annealed Cryo-R sample is mainly attributed to multiple strengthening mechanisms [36,37], including the grain boundary strengthening, dislocation strengthening, and solid solution strengthening. The detailed calculations can be seen in the Supplementary Materials. Moreover, a significant hetero-deformation-induced hardening exists among the heterogeneous domains, contributing to the additional strain-hardening ability for the improvement of strain hardening and tensile ductility. In contrast, the annealed Cold-R samples show small microstructural heterogeneity and a large average grain size, thus exhibiting limited strengthening modes and unattractive strength–ductility combinations.

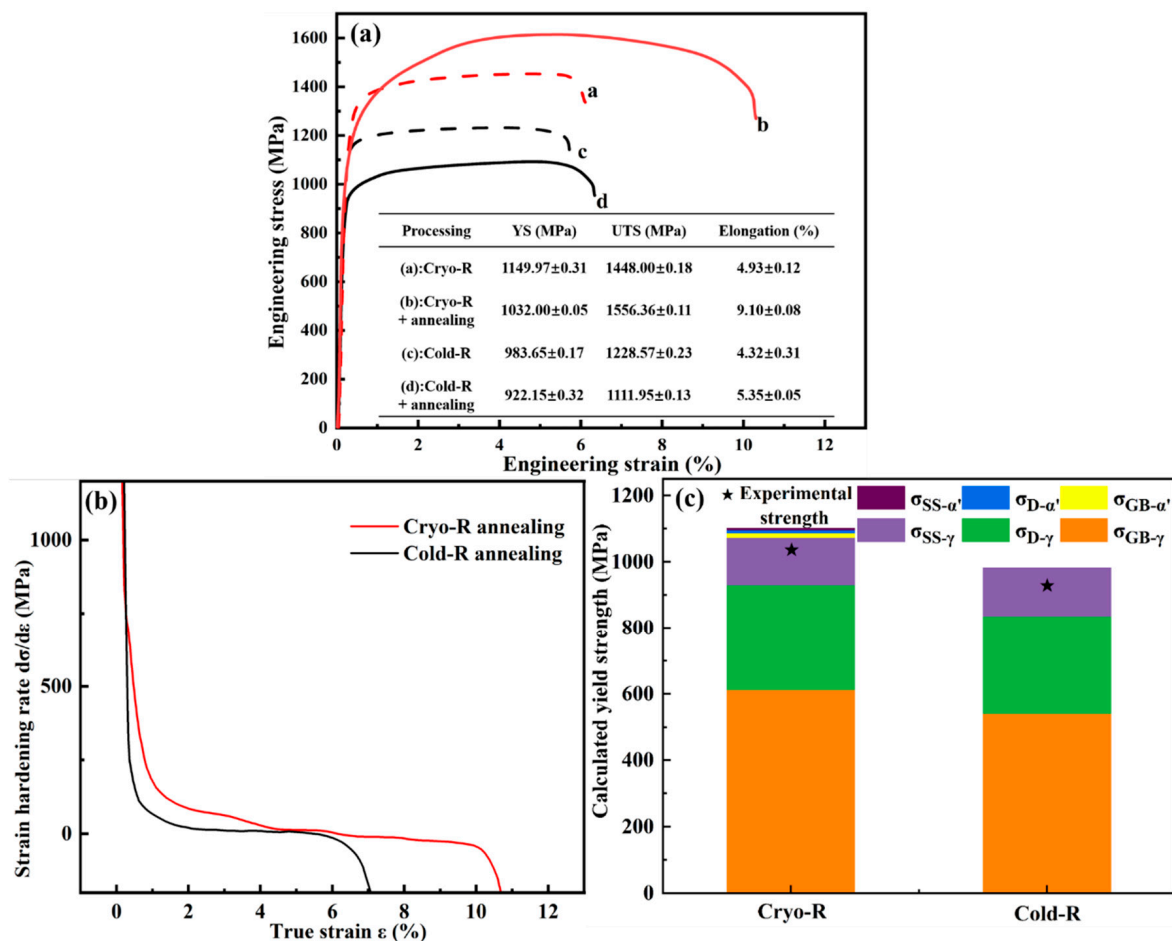


Figure 5. (a) Engineering stress–strain curves of the rolled and annealed SASS with Cryo-R and Cold-R processes (their tensile properties are shown in the inset table); (b) strain-hardening rate curve of Cryo-R/Cold-R annealing specimens; (c) calculated results of different strengthening mechanisms.

4. Conclusions

In summary, a good combination of strength and ductility was achieved in SASS by Cryo-R and subsequent annealing. The Cryo-R process resulted in the formation of a hierarchical multiple deformed substructure, including the dislocation cells, nanotwins and deformation-induced martensite, due to a low SFE and inhibited dislocation recovery. After annealing, the multiple precursors play an important role in obtaining the final heterogeneous structure, overcoming the strength–ductility trade-off. The high YS was mainly attributed to the ultra-fine microstructure, dislocation strengthening and retained martensite. Simultaneously, the hetero-deformation-induced hardening led to the improvement in strain hardening and tensile ductility.

Supplementary Materials: The following supporting information can be downloaded at: <https://www.mdpi.com/article/10.3390/ma16186298/s1>.

Author Contributions: Conceptualization, B.F., Y.L., W.G., Y.D. and D.T.; methodology, B.F., Y.G. and D.T.; validation, D.T.; formal analysis, B.F., Y.L., L.W. and D.T.; investigation, B.F.; data curation, D.T.; writing—original draft preparation, D.T.; writing—review and editing, B.F. and Y.L.; project administration, B.F. All authors have read and agreed to the published version of the manuscript.

Funding: This research received no external funding.

Institutional Review Board Statement: Not applicable.

Informed Consent Statement: Not applicable.

Data Availability Statement: The data are included in the text.

Conflicts of Interest: The authors declare that they have no known competing financial interest or personal relationships that could have appeared to influence the work reported in this paper.

References

1. Sunny, K.T.; Naik, K.N. A systematic review about welding of super austenitic stainless steel. *Mater. Today Proc.* **2021**, *47*, 41–44. [[CrossRef](#)]
2. Xin, H.; Zhuyun, W.; Lin, W.; Chen, C.; Fucheng, Z.; Wei, Z. Effect of pre-deformation on hot workability of super austenitic stainless steel. *J. Mater. Res. Technol.* **2022**, *16*, 66–75.
3. Zhang, Z.B.; Mishin, O.V.; Tao, N.R.; Pantleon, W. Microstructure and annealing behavior of a modified 9Cr–1Mo steel after dynamic plastic deformation to different strains. *J. Nucl. Mater.* **2015**, *458*, 458–463. [[CrossRef](#)]
4. Yan, F.K.; Liu, G.Z.; Tao, N.R.; Lu, K. Strength and ductility of 316L austenitic stainless steel strengthened by nano-scale twin bundles. *Acta Mater.* **2012**, *60*, 1059–1071. [[CrossRef](#)]
5. Tianyi, S.; Zhongxia, S.; Jaehun, C.; Jie, D.; Tongjun, N.; Yifan, Z.; Bo, Y.; Dongyue, X.; Jian, W.; Haiyan, W.; et al. Ultra-fine-grained and gradient FeCrAl alloys with outstanding work hardening capability. *Acta Mater.* **2021**, *215*, 215–223.
6. Li, W.L.; Tao, N.R.; Lu, K. Fabrication of a gradient nano-micro-structured surface layer on bulk copper by means of a surface mechanical grinding treatment. *Scr. Mater.* **2008**, *59*, 546–549. [[CrossRef](#)]
7. Li, J.; Mao, Q.; Nie, J.; Huang, Z.; Wang, S.; Li, Y. Impact property of high-strength 316L stainless steel with heterostructures. *Mater. Sci. Eng. A* **2019**, *754*, 457–460. [[CrossRef](#)]
8. Huang, C.X.; Hu, W.P.; Wang, Q.Y.; Wang, C.; Yang, G.; Zhu, Y.T. An Ideal Ultrafine-Grained Structure for High Strength and High Ductility. *Mater. Res. Lett.* **2014**, *3*, 88–94. [[CrossRef](#)]
9. Roy, B.; Kumar, R.; Das, J. Effect of cryorolling on the microstructure and tensile properties of bulk nano-austenitic stainless steel. *Mater. Sci. Eng. A* **2015**, *631*, 241–247. [[CrossRef](#)]
10. Wu, X.; Yang, M.; Yuan, F.; Wu, G.; Wei, Y.; Huang, X.; Zhu, Y. Heterogeneous lamella structure unites ultrafine-grain strength with coarse-grain ductility. *Proc. Natl. Acad. Sci. USA* **2015**, *112*, 14501–14505. [[CrossRef](#)]
11. Kalsar, R.; Ray, R.K.; Suwas, S. Effects of alloying addition on deformation mechanisms, microstructure, texture and mechanical properties in Fe-12Mn-0.5C austenitic steel. *Mater. Sci. Eng. A* **2018**, *729*, 385–397. [[CrossRef](#)]
12. Achmad, T.L.; Fu, W.; Chen, H.; Zhang, C.; Yang, Z.-G. Effects of alloying elements concentrations and temperatures on the stacking fault energies of Co-based alloys by computational thermodynamic approach and first-principles calculations. *J. Alloys Compd.* **2017**, *694*, 1265–1279. [[CrossRef](#)]
13. Fu, B.; Ge, Y.; Guan, W.; Guo, Y.; Wang, Z.; Ding, Y. Maintaining microstructure ultra-refinement in the austenitic stainless steel by inducing χ phase precipitating through severe cold rolling and annealing. *Mater. Res. Express* **2022**, *9*, 046515. [[CrossRef](#)]
14. Shu, J.; Wu, Y.; Ji, Y.; Chen, M.; Wu, H.; Gao, Y.; Wei, L.; Zhao, L.; Huo, T.; Liu, R. A new electrochemical method for simultaneous removal of Mn(2+) and NH(4)(+)-N in wastewater with Cu plate as cathode. *Ecotoxicol. Environ. Saf.* **2020**, *206*, 111341. [[CrossRef](#)]

15. Ye, K.L.; Luo, H.Y.; Lv, J.L. Producing Nanostructured 304 Stainless Steel by Rolling at Cryogenic Temperature. *Mater. Manuf. Process.* **2014**, *29*, 754–758. [[CrossRef](#)]
16. Xiong, Y.; Yue, Y.; Lu, Y.; He, T.; Fan, M.; Ren, F.; Cao, W. Cryorolling impacts on microstructure and mechanical properties of AISI 316 LN austenitic stainless steel. *Mater. Sci. Eng. A* **2018**, *709*, 270–276. [[CrossRef](#)]
17. Seol, J.-B.; Jung, J.E.; Jang, Y.W.; Park, C.G. Influence of carbon content on the microstructure, martensitic transformation and mechanical properties in austenite/ ϵ -martensite dual-phase Fe–Mn–C steels. *Acta Mater.* **2013**, *61*, 558–578. [[CrossRef](#)]
18. Lee, T.-H.; Kim, S.-J.; Jung, Y.-C. Crystallographic Details of Precipitates in Fe-22Cr-21Ni-6Mo(N) Superaustenitic Stainless Steels Aged at 900 °C. *Metall. Mater. Trans. A* **2000**, *31*, 13. [[CrossRef](#)]
19. Li, Z.; Fu, L.; Peng, J.; Zheng, H.; Shan, A. Effect of annealing on microstructure and mechanical properties of an ultrafine-structured Al-containing FeCoCrNiMn high-entropy alloy produced by severe cold rolling. *Mater. Sci. Eng. A* **2020**, *786*, 139446. [[CrossRef](#)]
20. Wang, H.; Shuro, I.; Umamoto, M.; Ho-Hung, K.; Todaka, Y. Annealing behavior of nano-crystalline austenitic SUS316L produced by HPT. *Mater. Sci. Eng. A* **2012**, *556*, 906–910. [[CrossRef](#)]
21. Zheng, C.; Liu, C.; Ren, M.; Jiang, H.; Li, L. Microstructure and mechanical behavior of an AISI 304 austenitic stainless steel prepared by cold- or cryogenic-rolling and annealing. *Mater. Sci. Eng. A* **2018**, *724*, 260–268. [[CrossRef](#)]
22. Li, J.; Gao, B.; Huang, Z.; Zhou, H.; Mao, Q.; Li, Y. Design for strength-ductility synergy of 316L stainless steel with heterogeneous lamella structure through medium cold rolling and annealing. *Vacuum* **2018**, *157*, 128–135. [[CrossRef](#)]
23. Mallick, P.; Tewary, N.K.; Ghosh, S.K.; Chattopadhyay, P.P. Microstructure-tensile property correlation in 304 stainless steel after cold deformation and austenite reversion. *Mater. Sci. Eng. A* **2017**, *707*, 488–500. [[CrossRef](#)]
24. Wang, W.; Yuan, F.; Jiang, P.; Wu, X. Size effects of lamellar twins on the strength and deformation mechanisms of nanocrystalline hcp cobalt. *Sci. Rep.* **2017**, *7*, 9550–9560. [[CrossRef](#)]
25. Wang, H.T.; Tao, N.R.; Lu, K. Strengthening an austenitic Fe–Mn steel using nanotwinned austenitic grains. *Acta Mater.* **2012**, *60*, 9–16. [[CrossRef](#)]
26. Zhao, L.; Qi, X.; Xu, L.; Han, Y.; Jing, H.; Song, K. Tensile mechanical properties, deformation mechanisms, fatigue behaviour and fatigue life of 316H austenitic stainless steel: Effects of grain size. *Fatigue Fract. Eng. Mater. Struct.* **2020**, *44*, 533–550. [[CrossRef](#)]
27. Singh, R.; Sachan, D.; Verma, R.; Goel, S.; Jayaganthan, R.; Kumar, A. Mechanical behavior of 304 Austenitic stainless steel processed by cryogenic rolling. *Mater. Today Proc.* **2018**, *5*, 16880–16886. [[CrossRef](#)]
28. Korznikova, G.; Mironov, S.; Konkova, T.; Aletdinov, A.; Zaripova, R.; Myshlyayev, M.; Semiatin, S. EBSD Characterization of Cryogenically Rolled Type 321 Austenitic Stainless Steel. *Metall. Mater. Trans.* **2018**, *49*, 16–23. [[CrossRef](#)]
29. Yan, F.K.; Tao, N.R.; Archie, F.; Gutierrez-Urrutia, I.; Raabe, D.; Lu, K. Deformation mechanisms in an austenitic single-phase duplex microstructured steel with nanotwinned grains. *Acta Mater.* **2014**, *81*, 487–500. [[CrossRef](#)]
30. Saeed-Akbari, A.; Imlau, J.; Prah, U.; Bleck, W. Derivation and Variation in Composition-Dependent Stacking Fault Energy Maps Based on Subregular Solution Model in High-Manganese Steels. *Metall. Mater. Trans. A* **2009**, *40*, 3076–3090. [[CrossRef](#)]
31. Huabing, L.; Zhouhua, J.; Hao, F.; Shucai, Z.; Peide, H.; Wei, Z.; Guoping, L.; Guangwei, F. Effect of Temperature on the Corrosion Behaviour of Super Austenitic Stainless Steel S32654 in Polluted Phosphoric Acid. *Int. J. Electrochem. Sci.* **2015**, *10*, 4832–4848.
32. Andersson, M.; Stalmans, R.; Gren, J.A. Unified Thermodynamic analysis of the stress-assisted $\gamma \rightarrow \epsilon$ martensitic transformation in Fe±Mn±Si alloys. *Acta Mater.* **1998**, *46*, 8. [[CrossRef](#)]
33. Wu, X.; Zhu, Y. Heterogeneous materials: A new class of materials with unprecedented mechanical properties. *Mater. Res. Lett.* **2017**, *5*, 527–532. [[CrossRef](#)]
34. Shi, Y.; Zhou, J. Analysis of mechanical behaviour of single-phase austenitic stainless steels based on microstructure deformation mechanism. *Micro Nano Lett.* **2019**, *14*, 1024–1028. [[CrossRef](#)]
35. Li, Y.S.; Tao, N.R.; Lu, K. Microstructural evolution and nanostructure formation in copper during dynamic plastic deformation at cryogenic temperatures. *Acta Mater.* **2008**, *56*, 230–241. [[CrossRef](#)]
36. Ma, K.; Wen, H.; Hu, T.; Topping, T.D.; Isheim, D.; Seidman, D.N.; Lavernia, E.J.; Schoenung, J.M. Mechanical behavior and strengthening mechanisms in ultrafine grain precipitation-strengthened aluminum alloy. *Acta Mater.* **2014**, *62*, 141–155. [[CrossRef](#)]
37. Wen, H.; Topping, T.D.; Isheim, D.; Seidman, D.N.; Lavernia, E.J. Strengthening mechanisms in a high-strength bulk nanostructured Cu–Zn–Al alloy processed via cryomilling and spark plasma sintering. *Acta Mater.* **2013**, *61*, 2769–2782. [[CrossRef](#)]

Disclaimer/Publisher’s Note: The statements, opinions and data contained in all publications are solely those of the individual author(s) and contributor(s) and not of MDPI and/or the editor(s). MDPI and/or the editor(s) disclaim responsibility for any injury to people or property resulting from any ideas, methods, instructions or products referred to in the content.